Materials Advances

PAPER

Check for updates

3D hierarchical rare-earth metal composite nanofiber membranes for highly durable and efficient photodegradations of organic pollutants†

Aditya Rianjanu, [iD] *[ad] Sephia Amanda Muhtar,[b] Hannah Faye M. Austria, [iD][c] Tarmizi Taher,[bd] Noto Susanto Gultom,[e] Wibawa Hendra Saputera, [iD][f] Hutomo Suryo Wasisto, [iD][g] Fatwa F. Abdi, [iD][h] Wei-Song Hung [iD][c] and Januar Widakdo*[i]

The use of powdered photocatalysts in wastewater treatment presents several challenges, such as difficulties in recovery, aggregation during use, and poor reusability, which limit their effectiveness in large-scale environmental applications. To address these issues, we developed sustainable and reusable photocatalytic membranes comprising three-dimensional (3D) hierarchical lanthanum-doped rare-earth metal oxide nanorods integrated onto polyacrylonitrile/polyvinylidene fluoride (PAN/PVDF) nanofibers (La-doped RE-NFs). These hybrid composite membranes were fabricated by combining electrospinning and hydrothermal synthesis methods. The La-doped RE-NFs not only possess a high surface-area-to-volume ratio but also demonstrate superior photocatalytic efficiency for removing common target organic pollutants in water (*i.e.*, Congo red (CR), methyl orange (MO), methylene blue (MB), and tetracycline (TC)). Here, the formation of the $CeCO_3F$ phase has contributed to the enhanced photocatalytic performance. From the kinetic analysis of the photocatalytic degradation, the rate constant (k) of La-doped RE-NFs in the MB removal test is 4.3 times higher than that of their undoped counterparts. Moreover, these proposed membranes exhibit excellent reusability, with only a ~5% reduction in degradation efficiency after five consecutive cycles. These findings highlight the potential of La-doped RE-NFs as a highly efficient and reusable photocatalytic membrane material for environmental applications, particularly in water treatment systems.

[a] *Department of Materials Engineering, Faculty of Industrial Technology, Institut Teknologi Sumatera, Terusan Ryacudu, Way Hui, Jati Agung, Lampung Selatan 35365, Indonesia. E-mail: aditya.rianjanu@mt.itera.ac.id*

[b] *Department of Environmental Engineering, Faculty of Infrastructure and Regional Technology, Institut Teknologi Sumatera, Terusan Ryacudu, Way Hui, Jati Agung, Lampung Selatan 35365, Indonesia*

[c] *Advanced Membrane Materials Research Center, Graduate Institute of Applied Science and Technology, National Taiwan University of Science and Technology, Taipei 10607, Taiwan, Republic of China*

[d] *Center for Green and Sustainable Materials, Institut Teknologi Sumatera, Terusan Ryacudu, Way Hui, Jati Agung, Lampung Selatan 35365, Indonesia*

[e] *Department of Physics, Faculty of Mathematics and Natural Sciences, Universitas Padjadjaran, Jalan Raya Bandung-Sumedang 11, 45363, Indonesia*

[f] *Department of Chemical Engineering, Faculty of Industrial Technology, Institut Teknologi Bandung, Jl. Ganesha 10, Bandung, 40132, Indonesia*

[g] *PT Nanosense Instrument Indonesia, Yogyakarta 55167, Indonesia*

[h] *School of Energy and Environment, City University of Hong Kong, 83 Tat Chee Avenue, Kowloon, Hong Kong SAR, China*

[i] *Department of Physics, Faculty of Mathematics and Natural Sciences, Universitas Indonesia, Depok 16424, Indonesia. E-mail: januar.widakdo@sci.ui.ac.id*

† Electronic supplementary information (ESI) available. See DOI: https://doi.org/10.1039/d4ma01144a

Introduction

Photocatalysis has gained widespread attention as a sustainable and efficient solution for addressing environmental pollution, particularly for the degradation of organic pollutants in water systems.[1,2] By utilizing light energy, photocatalysts can generate reactive species such as superoxide radicals ($\bullet O_2^-$) and hydroxyl radicals ($\bullet OH$), which can degrade a wide range of contaminants (*e.g.*, dyes, pharmaceuticals, and industrial waste chemicals) into harmless by-products.[3–5] The potential to use renewable energy sources, such as sunlight, makes photocatalysis an environmentally friendly and energy-efficient approach to water treatment, aligning with global efforts to develop green technologies.[6,7]

A wide range of compounds, such as metal oxides[8] (*e.g.*, titanium dioxide (TiO_2),[9] zinc oxide (ZnO),[10] iron oxide (Fe_2O_3),[11,12] tungsten trioxide (WO_3),[13,14] niobium pentoxide (Nb_2O_5),[15–17] and cerium oxide (CeO_2)),[18–21] carbon,[22,23] bismuth oxyhalides (*e.g.*, bismuth oxychloride (BiOCl), bismuth oxybromide (BiOBr), and bismuth oxyiodide (BiOI)[24,25]), and

metal–organic frameworks (MOFs),[26,27] have been studied as photocatalytic materials due to their high photocatalytic activity, chemical stability, and versatility. Despite their promising properties and high performance in water treatment applications, these materials often face challenges related to aggregation, recovery, and reusability because of their predominant use as powders.[28,29] Powder-based photocatalysts tend to agglomerate during reactions, reducing their surface area and activity.[30,31] Moreover, recovering and reusing these powders after each cycle can be difficult and costly, often leading to performance degradation over time.[32]

Several strategies have been developed to address these limitations and improve the reusability of photocatalysts, including immobilizing photocatalytic materials on solid supports[33,34] or incorporating them into membrane structures.[35,36] One promising approach is the development of photocatalytic membranes, where the catalytic material is directly embedded within or coated onto stable substrates, such as nanofibers.[37,38] Photocatalytic membranes offer distinct advantages over their powder-based counterparts in terms of easier recovery and enhanced stability during repeated use.[37,38] Nanofiber-based membranes, fabricated through electrospinning techniques, have emerged as an effective platform for photocatalysis.[39,40] These membranes provide a high surface-area-to-volume ratio, tunable porosity, and improved light absorption, making them highly efficient for environmental applications. Integrating metal oxides or other photocatalytic materials into nanofibers allows the resulting composite membranes to maintain high catalytic activity while being easily separated and reused, significantly improving their practicality for long-term water treatment applications.

Building on these advancements, we focus on developing sustainable photocatalytic membranes that not only deliver high photodegradation efficiency of organic pollutants but also offer high reusability. Here, three-dimensional (3D) hierarchical rare-earth metal oxide composite nanofibers were fabricated by combining electrospinning and hydrothermal synthesis techniques.

As a base platform to grow lanthanum (La)-doped metal oxide nanorods, polyacrylonitrile/polyvinylidene fluoride (PAN/PVDF) nanofibers were selected because of their excellent mechanical strength, chemical resistance, and flexibility, which are ideal for water treatment applications. Besides optimizing the hydrothermal growth process of the composite materials, we assessed the performance and practical use of the proposed hybrid membranes towards various organic pollutants of dyes and antibiotics (i.e., Congo red (CR), methyl orange (MO), methylene blue (MB), and tetracycline (TC)) by characterizing their degradation efficiency and long-term stability.

Materials and methods

Materials

Polymers of polyacrylonitrile (PAN, M_w = 150 000 g mol^{-1}) and polyvinylidene fluoride (PVDF, M_w = 530 000 g mol^{-1}) purchased from Sigma-Aldrich, Singapore, were used for the nanofiber preparations. N,N-Dimethyl formamide (DMF) obtained from Merck, Germany, was employed as a solvent in the electrospinning process. For the fabrication of the rare-earth metal oxide nanostructures, we used cerium nitrate hexahydrate (Ce(NO$_3$)$_3$·6H$_2$O), lanthanum nitrate hexahydrate (La(NO$_3$)$_3$·6H$_2$O), and urea (NH$_2$CONH$_2$), which were purchased from Merck, Germany. The tested organic pollutants of Congo red (CR, C.I. 22120), methyl orange (MO, C.I. 13025), methylene blue (MB, C.I 52015) dye, and tetracycline hydrochloride (TC-HCl) were also obtained from Merck, Darmstadt, Germany. All materials were used as received without any further purification.

Composite nanofiber fabrication

The fabrication steps of the 3D hierarchical rare-earth metal oxide composite nanofiber membranes are illustrated in Fig. 1. These are basically divided into two main processes (i.e., electrospinning and hydrothermal synthesis). First, the

Fig. 1 Fabrication process steps for three-dimensional (3D) hierarchical rare-earth metal oxide composite nanofiber membranes. Electrospinning and hydrothermal synthesis methods are used to create polyacrylonitrile/polyvinylidene fluoride (PAN/PVDF) nanofibers and grow rare-earth metal oxide nanorods on them, respectively.

polyacrylonitrile/polyvinylidene fluoride (PAN/PVDF) nanofibers were synthesized using an electrospinning machine (ILMI-N101 Electrospinning, ILMI laboratory, Bandung, Indonesia). The electrospinning procedures were adapted from those reported in the literature.[15,41] 10 mL of PAN/PVDF solution was used to prepare each nanofiber membrane. Here, the electrospinning parameters were set as a high voltage of 9 kV, a tip-to-collector distance of 10 cm, and a feed rate of 0.4 mL h^{-1}. The PAN/PVDF nanofiber membrane was then cut into a size of 5 × 10 cm^2 and subsequently put inside a hydrothermal autoclave reactor.

Second, to prepare for the hydrothermal synthesis, 6.0 g of cerium nitrate hexahydrate (Ce(NO$_3$)$_3$·6H$_2$O) and 4.2 g of urea were dissolved in 70 mL of deionized water under continuous stirring with a magnetic stirrer until a homogeneous solution was achieved. To fabricate La-doped composite nanofibers, 0.36 g of lanthanum nitrate hexahydrate (La(NO$_3$)$_3$·6H$_2$O) was added as the doping agent. The resulting mixture was transferred to a Teflon-lined stainless-steel autoclave, which was then sealed and subjected to hydrothermal treatment at 180 °C for 72 hours. After the hydrothermal reaction, the resulting membrane was thoroughly washed with deionized water to remove any residual reactants and impurities. The membrane was then dried in an electric oven at 60 °C for 6 hours to ensure complete water removal.

Three types of membrane samples were prepared to compare and evaluate the photocatalytic performances of different membrane architectures. The first membrane sample is the PAN/PVDF nanofibers without any metal oxide nanostructures (*i.e.*, NFs). The second and third membrane samples are the PAN/PVDF nanofibers that are integrated with undoped (*i.e.*, RE-NFs) and La-doped rare earth metal oxide nanorods (*i.e.*, La-doped RE-NFs), respectively. For the case of RE-NFs, these nanofibers were prepared using an identical fabrication process as that used for La-doped RE-NFs, but without the addition of lanthanum nitrate during the hydrothermal procedure.

Material characterizations

The morphology and surface elemental composition of the nanofiber membranes were analyzed using field-emission scanning electron microscopy (FE-SEM, Model 6500F, JEOL, Ltd, Japan) equipped with energy-dispersive X-ray spectroscopy (EDS). Wide-angle X-ray diffraction (XRD) measurements were carried out on a D8 DISCOVER SSS, Bruker, Germany, to examine the crystalline structure of the samples. Fourier-transform infrared (FTIR) spectroscopy was conducted with a Shimadzu IRSpirit-X Compact FTIR Spectrometer to investigate the functional groups present in the nanofibers. Thermogravimetric analysis (TGA) was performed using a Shimadzu TA-60 to assess the thermal characteristics of the PAN/PVDF nanofibers following the hydrothermal treatment. An X-ray photoelectron spectroscopy (XPS, Model K-Alpha, Thermo Fisher, USA) was employed to analyze the elemental composition and chemical bonding within the nanofiber membrane. Photoluminescence (PL, PTI QuantaMaster™ 30, from Horiba, excitation wavelength (λ_{ex} = 300 nm) spectroscopy was used to evaluate the optical

emission properties, and UV-vis spectrophotometry (Thermo Fisher Scientific, Evolution 220) in diffuse reflectance spectra (DRS) mode was employed to further explore the optical absorption characteristics of the as-prepared samples.

Photocatalytic degradation measurements

The photocatalytic degradation experiments were performed using four different model organic pollutants, *i.e.*, cationic dye (MB), anionic dyes (CR and MO), and antibiotic (TC). Each pollutant solution was prepared at a concentration of 10 ppm in 100 mL of distilled water. For each experiment, 0.05 g of the photocatalytic membrane sample (*i.e.*, NFs, RE-NFs, or La-doped RE-NFs) was dispersed in the pollutant solution. The suspension was stirred in the dark for 30 minutes to evaluate any adsorption behaviour and establish adsorption–desorption equilibrium before UV light irradiation. Any significant reduction in pollutant concentration during this phase would indicate adsorption of the pollutants onto the nanofiber membrane. Subsequently, the suspension was irradiated with UV light using four Phillips UVC lamps (10 W, $\lambda \approx$ 253.7 nm) for 120 minutes. The detailed photocatalytic experimental setup including the lamp and pollution distance is shown in Fig. S1 (ESI†). During the dark phase, 3 mL aliquots were taken every 10 minutes to measure adsorption, and after UV light exposure began, samples were collected at 30-minute intervals to monitor photocatalytic degradation. The concentration of the collected samples was analysed using a Shimadzu UV1280 UV-vis spectrophotometer. The maximum absorbance wavelengths for each pollutant were measured as follows: CR (497 nm), MO (464 nm), MB (664 nm), and TC (357 nm). The absorbance data were used to calculate the remaining concentration of pollutants over time, providing insights into both adsorption behaviour and photocatalytic degradation efficiency.

Results and discussion

Hierarchical rare-earth metal composite nanofiber membrane characteristics

From the electrospinning process, the resulting electrospun plain PAN/PVDF nanofibers (*i.e.*, NFs) have a smooth and homogeneous structure with a diameter of ∼710 nm (see Fig. 2(a)). Upon the hydrothermal growth of the rare-earth metal oxide, flower-like structures consisting of nanorods ranging from hundreds to thousands of nanometers appeared on the nanofiber surfaces (*i.e.*, RE-NFs), as depicted in Fig. 2(b). These nanorods, having a diameter of ∼900 nm, were evenly distributed across the nanofiber surface, as indicated by the yellow arrows in Fig. 2(b) and (c). This indicates that the nanorods grew directly on the nanofiber surfaces, as further highlighted by the yellow-circled areas in Fig. 2(c), confirming the structural integrity of the underlying nanofiber template.[42,43] At higher magnifications, a sheet-like structure was observed, distinct from both the nanofiber and nanorod formations, further emphasizing the hierarchical nature of the composite material. These 3D hierarchical structures could
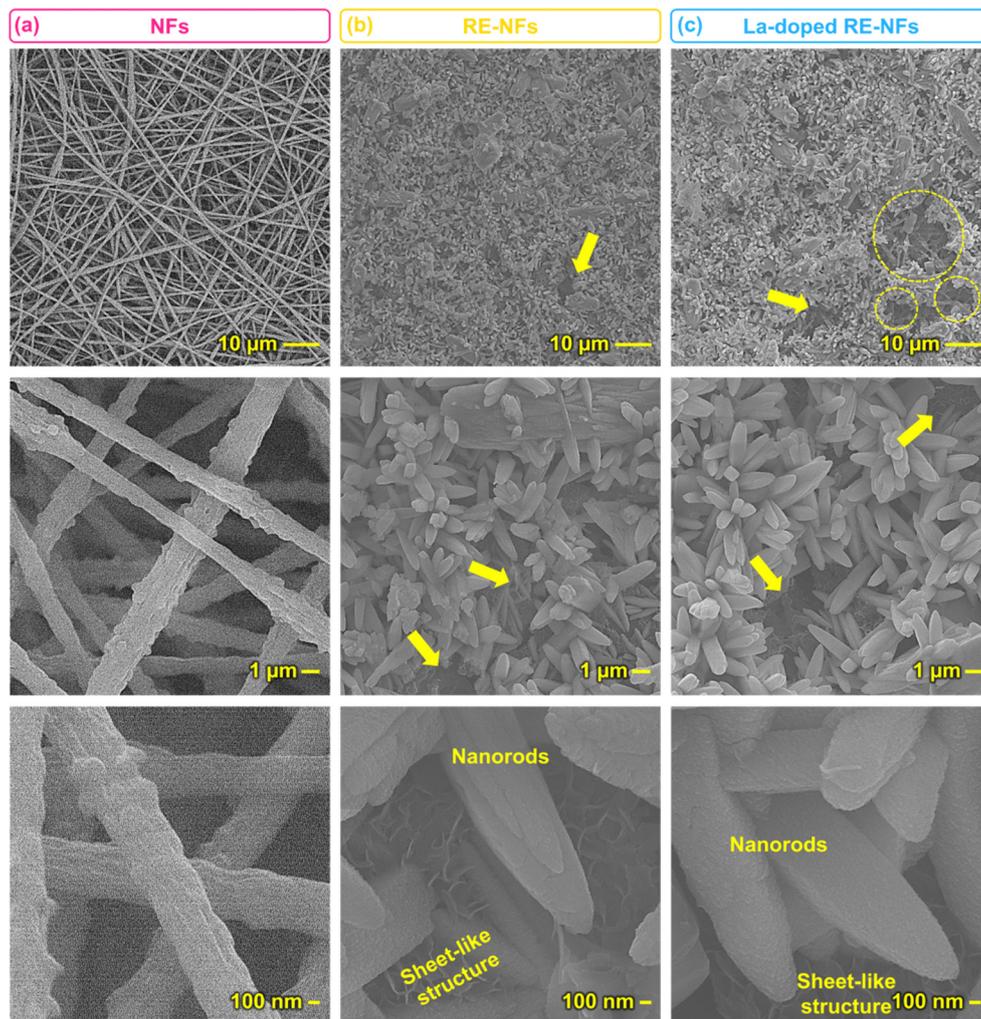
Fig. 2 Scanning electron microscopy (SEM) images showcasing the morphology of composite nanofiber membranes at different magnifications. (a) Plain PAN/PVDF nanofibers (NFs). 3D hierarchical rare-earth metal oxide composite nanofibers (b) without (RE-NFs) and (c) with lanthanum doping (La-doped RE-NFs). The images show the presence of nanorods on the surfaces of the RE-NFs and La-doped RE-NFs.

enhance the surface area, which is crucial for catalytic and adsorption applications.[44] Furthermore, Fig. 1 presents a photograph of all nanofiber samples, visually confirming that the membrane structure remains intact following hydrothermal treatment, with the only noticeable change being a shift in nanofiber color. Following the lanthanum doping, the overall morphology of the La-doped RE-NFs shown in Fig. 2(c) remains consistent with that of the undoped samples (RE-NFs). The surface textures, including the distribution of nanorods, did not exhibit any significant changes due to the doping process. This suggests that while La doping may introduce chemical or functional modifications, it does not drastically alter the microstructure of the nanofibrous mats.

In the EDS elemental mapping of RE-NFs (Table S1, ESI†) and La-doped RE-NFs (see Fig. 3(a)), the measured elements include carbon (C), nitrogen (N), oxygen (O), fluorine (F), cerium (Ce), and lanthanum (La). Here, although Ce (70.18 wt% and 21.23 at%) and O (15.31 wt% and 40.56 at%) are the dominant elements, the presence of C (6.58 wt% and 23.24 at%) and F

(6.48 wt% and 14.46 at%) is also significant, indicating the retention of the organic components, which is a typical characteristic of hierarchical composite nanofibers.[45,46] Furthermore, a very small percentage of La (1.42 wt% and 0.43 at%) was also observed, suggesting the successful doping of La into the RE-NFs.

The X-ray diffractograms of composite nanofibers are shown in Fig. 3(b). The results reveal that $CeCO_3F$ is the dominant phase in all composite nanofibers rather than simple CeO_2 cubic structures in contrast with previous findings.[18,19] This was unexpected since typically hydrothermal growth on top of the nanofiber membrane results in materials similar to the process without membrane template.[47–49] The $CeCO_3F$ phase was identified according to the PDF#11-0340.[50,51] While $CeCO_3F$ was not intentionally designed in this study, its formation presents an intriguing finding. Several previous reports in literature indicate that $CeCO_3F$ has been explored in various applications, including NH_3-SCR denitrification catalysis,[52] luminescence,[53] and as a precursor for CeO_2 synthesis,[50] demonstrating its significance in
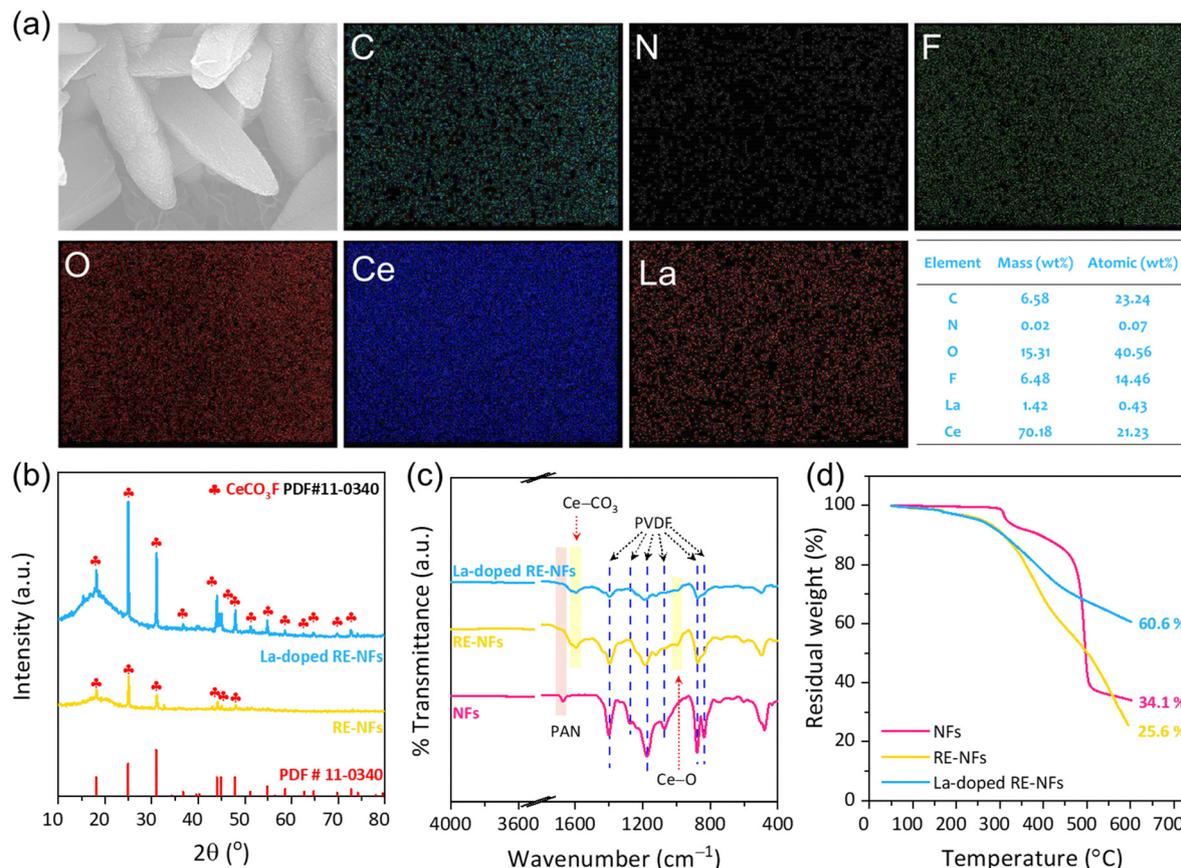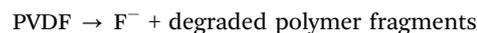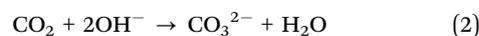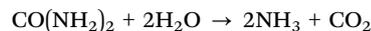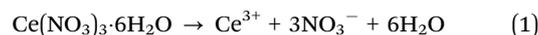
Fig. 3 Comprehensive material characterizations of composite nanofiber membranes. (a) Energy-dispersive X-ray spectroscopy (EDS) results of La-doped RE-NFs, showing the elemental mappings of C, N, O, F, La, and Ce elements. (b) X-ray diffractograms of NFs, RE-NFs, and La-doped RE-NFs. (c) Fourier-transform infrared (FTIR) spectra displaying characteristic peaks across all three samples. (d) Thermogravimetric analysis (TGA) curves showing the thermal degradation behaviors for all nanofiber types (NFs, RE-NFs, and La-doped RE-NFs).

advanced materials. Those studies highlight its oxygen storage properties, stability, and potential catalytic activity, suggesting that $CeCO_3F$ could contribute to the photocatalytic performance observed in our study.[50,52,53]

To understand the growth of the $CeCO_3F$ phase on the nanofiber surfaces, the chemical reaction in each processing step needs to be analyzed. Firstly, during the dissolution of cerium nitrate hexahydrate and urea using DI water, the cerium (Ce^{3+}) and carbonate CO_3^{2-} ions were formed (see eqn (1) and (2)). Secondly, during the hydrothermal process, the formation of cerium carbonate precipitate ($Ce_2(CO_3)_3$) started to occur (eqn (3)). Simultaneously, due to the harsh hydrothermal conditions, partial degradation of PVDF may occur releasing fluoride ions (F^-) and further reacting with the cerium carbonate to form cerium oxyfluorocarbonate ($CeCO_3F$) according to eqn (4). The nucleation and growth of the $CeCO_3F$ had then continuously occurred on the nanofiber surfaces until the hydrothermal synthesis was finished. This finding is also consistent with the EDS results in the previous section, showing that the major elements found on the membrane surface were C, O, F, and Ce. In addition to these findings, the La-doped RE-NFs displayed key differences compared to the undoped ones (RE-NFs). Specifically, the La-doped nanofibers exhibited much sharper and more well-defined

peaks in the XRD patterns, indicating greater crystallinity of the $CeCO_3F$ phase. This could suggest that the presence of La facilitates more ordered growth of the $CeCO_3F$ structure on the nanofiber surfaces.

$$Ce(NO_3)_3 \cdot 6H_2O \rightarrow Ce^{3+} + 3NO_3^- + 6H_2O \quad (1)$$

$$CO(NH_2)_2 + 2H_2O \rightarrow 2NH_3 + CO_2$$

$$NH_3 + H_2O \rightarrow NH_4^+ + OH^-$$

$$CO_2 + 2OH^- \rightarrow CO_3^{2-} + H_2O \quad (2)$$

$$2Ce^{3+} + 3CO_3^{2-} \rightarrow Ce_2(CO_3)_3 \quad (3)$$

$$PVDF \rightarrow F^- + \text{degraded polymer fragments}$$

$$Ce_2(CO_3)_3 + 2F^- \rightarrow 2CeCO_3F + CO_3^{2-} \quad (4)$$

FTIR spectroscopy was utilized to elucidate the molecular structure of the composite nanofibers, as depicted in Fig. 3(c). The FTIR spectra confirmed the successful fabrication of the PAN/PVDF nanofibers, exhibiting characteristic peaks

typical for such materials.[54,55] The peak at 1668 cm^{-1}, attributed to the C=O stretching vibration from carbonyl groups, which was likely formed due to oxidation of the nitrile groups (C≡N) in PAN,[56,57] diminished in intensity after the hydrothermal growth of rare-earth metal oxide in both samples of undoped RE-NFs and La-doped RE-NFs. This change suggests a reduction or alteration of the carbonyl groups upon metal oxide incorporation. Characteristic absorption bands of the β-phase of PVDF were prominent in the spectra of the PAN/PVDF samples, observed mainly at 1400, 1275, 1175, 1070, 876, and 836 cm^{-1}.[54,55] While some β-PVDF peaks persisted in the composite nanofibers, their intensities were reduced, indicating that portions of the organic components remained intact within the composite structure. New peaks emerged in the spectra of both undoped RE-NFs and La-doped RE-NFs, enhancing our understanding of the chemical modifications induced by the doping process. The peak at 1587 cm^{-1} likely indicates the formation of metal–carboxylate complexes,[58] specifically cerium carbonate (CeCO$_3$), as corroborated by XRD analysis. Another significant peak at 992 cm^{-1} is attributed to metal–oxygen stretching vibrations, predominantly the Ce–O bond, with potential minor contributions from La–O bonds in the doped variants.[59]

The thermogravimetric analysis (TGA) results depicted in Fig. 3(d) reveal the thermal stability and decomposition characteristics of the nanofiber samples (*i.e.*, NFs, RE-NFs, and La-doped RE-NFs), providing insights into their composition. The NFs exhibited a residual weight of 34.1% at 600 °C, which primarily represents the fraction of thermally stable inorganic components and the carbonized remnants of the PAN/PVDF polymer matrix.[60,61] In contrast, RE-NFs showed a lower residual weight of 25.6%, suggesting that the incorporation of rare-earth metal oxides in this form slightly decreases thermal stability, possibly due to structural modifications or interactions between the polymer matrix and metal oxides affecting the degradation behavior. Notably, La-doped RE-NFs displayed the highest thermal stability, with a residual weight of 60.6% at 600 °C, indicating that lanthanum incorporation significantly enhances the material's thermal resistance, likely due to the formation of more stable inorganic phases and improved polymer–metal oxide interactions. By comparing the residual weight percentages, we can estimate the relative composition of PAN/PVDF (~73.5%) and rare-earth metal part (~26.5%), where the increased residual mass in La-doped RE-NFs suggests a higher content of thermally stable inorganic components, while the lower residual weight in RE-NFs implies a higher fraction of organic decomposition.[62,63] These findings highlight the crucial role of rare-earth metal incorporation, particularly lanthanum doping, in modifying the composition, stability, and overall material properties of the nanofibers, further supporting their potential application in photocatalytic processes.

The lanthanum doping likely promotes the formation of more stable chemical bonds within the nanofiber structure, making them more resistant to thermal degradation and underlining the beneficial impact of La incorporation on both the photocatalytic and thermal performances of the nanofibers. Interestingly, both RE-NFs and La-doped RE-NFs exhibited an earlier onset of thermal degradation compared to the NFs. This could be attributed to the introduction of rare-earth metal oxides, which might alter the chemical interactions within the nanofibers. The incorporation of cerium and lanthanum compounds could introduce local stresses or defects in the polymer matrix, causing the composite to begin decomposing at lower temperatures. Additionally, the partial degradation of the PVDF polymer under hydrothermal conditions, particularly in the La-doped RE-NFs, may introduce weaker points in the fiber structure, leading to earlier degradation.

The XPS survey spectra displayed in Fig. 4(a) show that the NF sample exhibits a composition consistent with reference PAN/PVDF nanofibers, featuring prominent peaks for C 1s, O 1s, N 1s, and F 1s.[64,65] This observation confirms that the NF sample retains the expected elemental profile for PAN/PVDF nanofibers, with carbon (C), nitrogen (N), oxygen (O), and fluorine (F) as primary constituents. In contrast, the RE-NFs and La-doped RE-NFs samples reveal additional peaks in the Ce 3d, indicating the successful incorporation of cerium into the nanofiber matrix.[66] The presence of these rare-earth elements distinguishes the modified samples from the original PAN/PVDF structure and is consistent with the anticipated doping process. Furthermore, the relative intensity of the F 1s peak appears slightly diminished in the RE-NFs and La-doped RE-NFs samples, suggesting potential interactions between fluorine and the introduced rare-earth elements, possibly due to changes in the PVDF structure induced by doping.

The high-resolution C 1s spectra shown in Fig. 4(b) for NFs, RE-NFs, and La-doped RE-NFs reveal distinct differences in the chemical environments of carbon within each sample. For the NFs, the C 1s spectrum primarily displays peaks associated with C–C and C–F bonds, typical of the PAN/PVDF matrix. However, in the RE-NFs and La-doped RE-NFs samples, additional peaks appear around 287–288 eV, corresponding to C=O and C–O bonds, indicating the presence of surface oxidation or the formation of carbonyl functionalities.[67] This observation suggests that the hydrothermal process involved in rare-earth modification introduces oxygen-containing groups on the nanofiber surface, contributing to the observed shifts and additional peaks in the C 1s spectra for the modified samples.

In the high-resolution N 1s, F 1s, and Ce 3d spectra (Fig. 4(c)–(e), respectively), further distinctions between the samples are evident. The N 1s spectrum for NFs shows a characteristic peak associated with C≡N from PAN.[68,69] In contrast, the F 1s spectra of RE-NFs and La-doped RE-NFs reveal a shift in the C–F peak, potentially indicating interactions between fluorine and the rare-earth elements, particularly cerium and lanthanum, forming M–F bonds.[70,71] The Ce 3d spectrum in RE-NFs and La-doped RE-NFs exhibits multiple peaks indicative of Ce^{3+} and Ce^{4+} oxidation states, confirming the presence of cerium in mixed oxidation states.[72–74] These chemical shifts and additional peaks in the modified samples underscore the influence of rare-earth doping on the electronic and chemical environments of the nanofiber membranes,
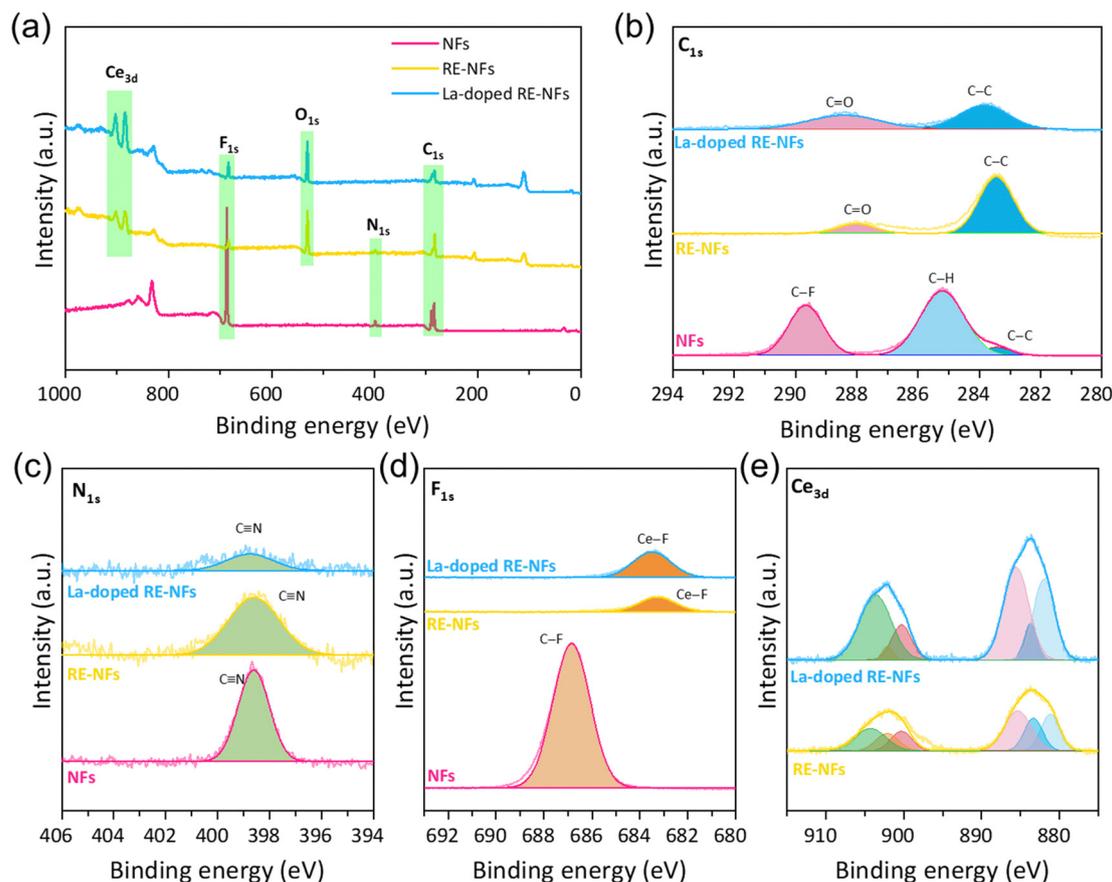
Fig. 4 XPS spectra of NFs, RE-NFs, and La-doped RE-NFs. (a) Survey spectrum displaying the elemental composition with highlighted peaks for Ce 3d, F 1s, O 1s, C 1s, and N 1s, confirming successful integration of rare-earth elements. The high-resolution spectra for (b) C 1s, (c) N 1s, (d) F 1s, and (e) Ce 3d provide detailed insights into the chemical states of each element in the prepared samples.

suggesting enhanced surface functionality that can be advantageous for photocatalytic applications.

Photocatalytic degradation performance

Fig. 5 provides a comprehensive overview of the degradation performances and kinetics of the composite nanofibers (NFs, RE-NFs, and La doped RE-NFs) against four organic pollutants (*i.e.*, CR, MO, MB, and TC). The UV-vis spectroscopy data of the various pollutants during the photocatalysis experiment are shown in Fig. S2 (ESI†). Fig. 5(a)–(d) depict the concentration decay over time, where the relative concentration (C/C_0) decreases more sharply for La-doped RE-NFs compared to NFs and RE-NFs. This suggests that the La-doped RE-NFs have a faster degradation rate for all tested pollutants. In the dark condition (−30 to 0 min), no significant changes in pollutant concentration were observed for the CR, MO, and TC samples, indicating minimal adsorption onto the nanofiber membranes. However, in the MB sample, a noticeable reduction in concentration was detected during the dark phase, especially for RE-NFs and La-doped RE-NFs samples, suggesting that an adsorption process might have occurred prior to the photocatalytic degradation for those photocatalytic membranes.

Fig. 5(e)–(h) show the $\ln(C_0/C)$ plots, confirming the first-order kinetics of the degradation process for all four pollutants

(CR, MO, MB, and TC). The kinetic analysis of the degradation process was performed using the linearized form of the first-order reaction model accordance to eqn (5):

$$\ln(C_0/C) = kt \qquad (5)$$

where C_0 is the initial concentration of the pollutant, C is the concentration at time t, and k is the rate constant.[75,76] The linearity of the $\ln(C_0/C)$ plots, as seen in Fig. 5(e)–(h), confirms that the photocatalytic degradation of all four pollutants follows first-order kinetics. The La-doped RE-NFs consistently display steeper slopes in the $\ln(C_0/C)$ plots compared to NFs and RE-NFs, indicating significantly faster degradation rates across all pollutants. The first-order rate constants (k) were calculated from the slopes of the $\ln(C_0/C)$ *versus* time plots and are presented in Fig. 6(i)–(l). They presented in the form of the rate constant per gram of catalyst ($\text{min}^{-1}\ \text{g}^{-1}$) for more meaningful comparison. For the La-doped RE-NFs, the rate constants are notably higher across all pollutants, demonstrating enhanced photocatalytic activity. For instance, in the case of CR pollutant, the rate constant for La-doped RE-NFs is approximately 0.151 $\text{min}^{-1}\ \text{g}^{-1}$, which is higher than those for NFs (0.108 $\text{min}^{-1}\ \text{g}^{-1}$) and RE-NFs (0.109 $\text{min}^{-1}\ \text{g}^{-1}$). Similar trends are observed for MO, MB, and TC pollutants, where La-doped
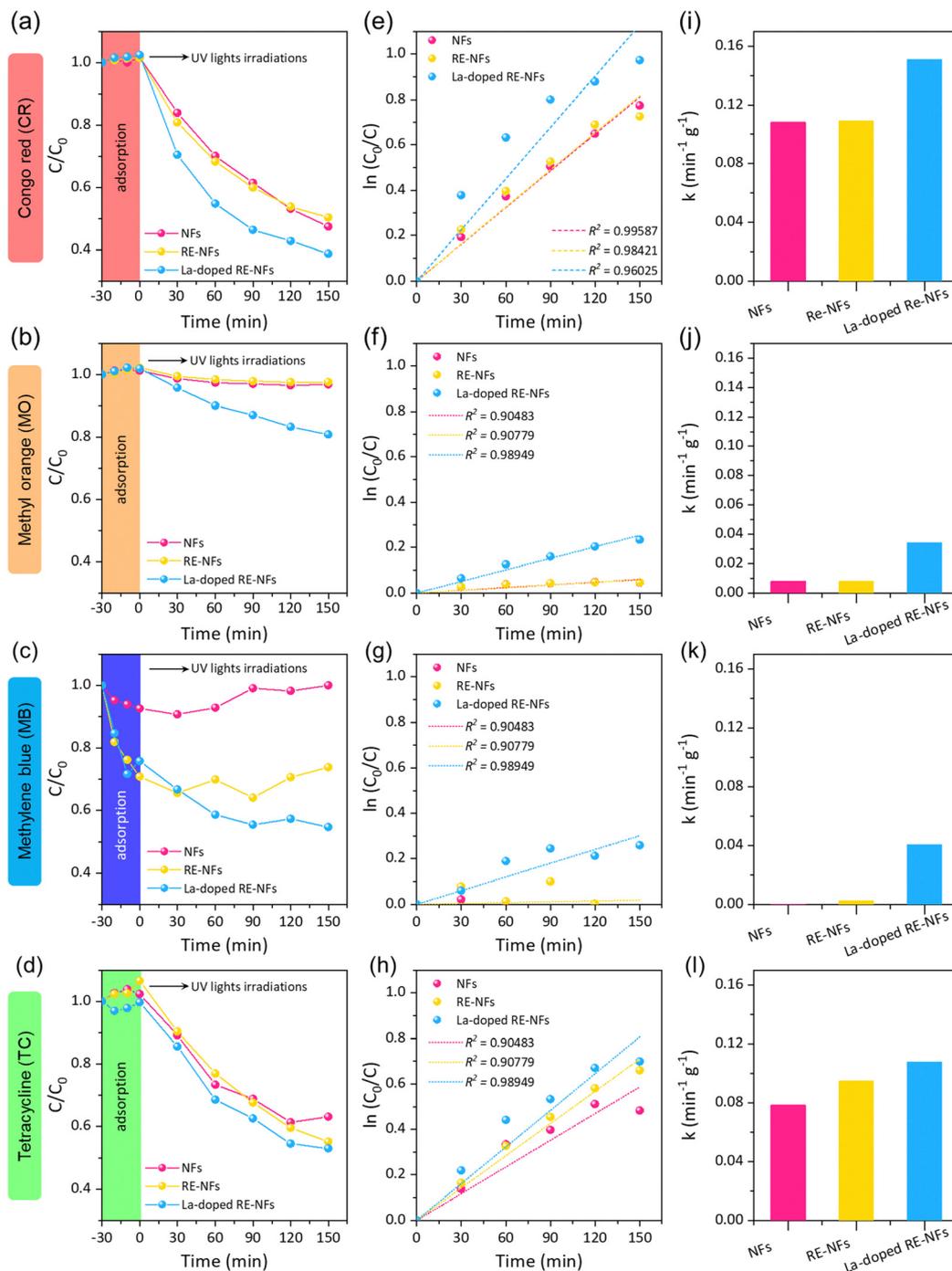
Fig. 5 Photocatalytic degradation performances and kinetics of composite nanofiber membranes towards various organic pollutants. Degradation curves showing concentration decay over time for (a) Congo red (CR), (b) methyl orange (MO), (c) methylene blue (MB), and (d) tetracycline (TC). First-order kinetic plots for the degradations of (e) CR, (f) MO, (g) MB, and (h) TC. Corresponding rate constants (k) for the degradations of (i) CR, (j) MO, (k) MB, and (l) TC. All the three samples of NFs, RE-NFs, and La doped RE-NFs were measured, and their results were evaluated.

RE-NFs exhibit the highest rate constants. The rate constants of the La-doped RE-NFs have increased up to 1.4, 4.3, 4.1, and 1.4-fold from those of their previous NFs for CR, MO, MB, and TC pollutants, respectively. This substantial increase in the rate constants highlights the effectiveness of lanthanum doping in accelerating the degradation process and improving the overall photocatalytic efficiency of the composite nanofibers.

The La-doped RE-NFs developed in this study achieved a normalized degradation rate of 0.15 min^{-1} g^{-1} for Congo red (CR) using a 4 × 10 W UV lamp, demonstrating efficient photocatalytic activity under moderate UV light conditions. The performance comparison of the as-prepared La-doped RE-NFs to previous photocatalysts integrated into nanofiber matrices is available in Table 1.[15,77–84] This performance is
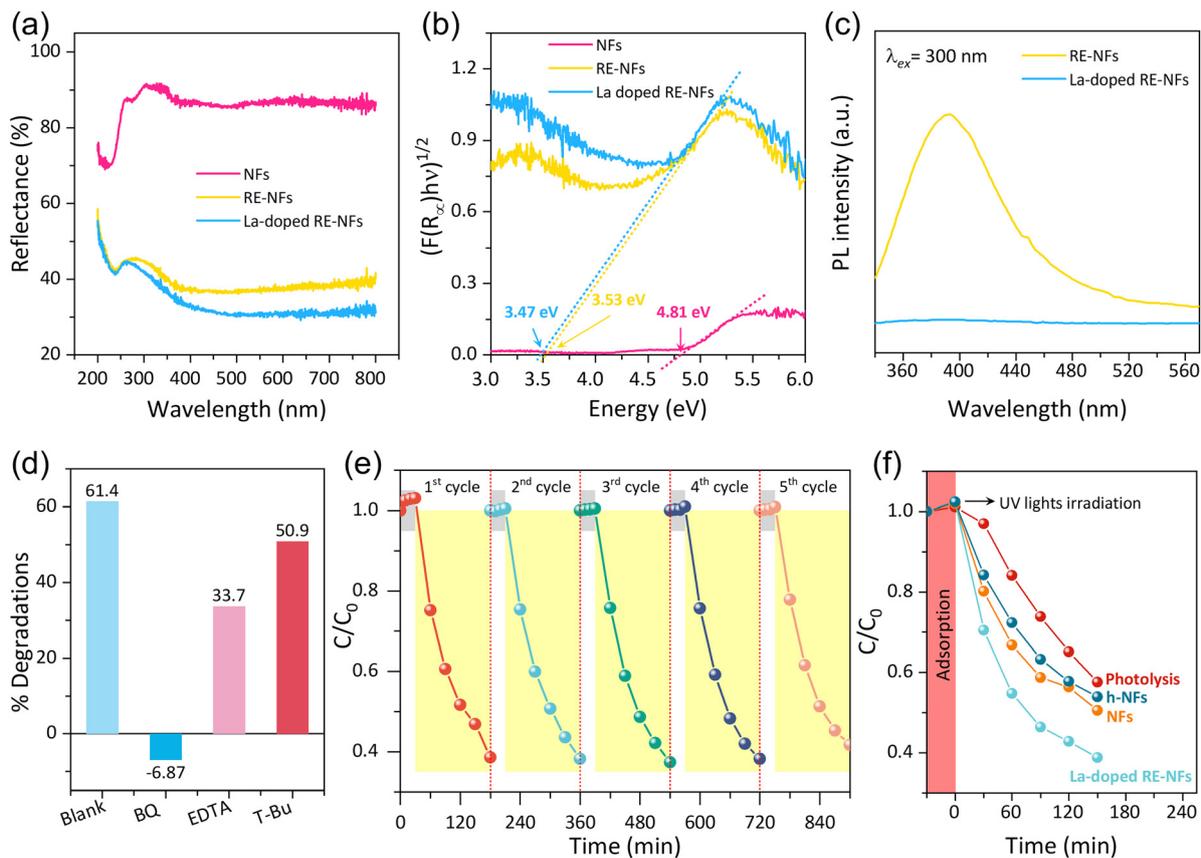
Fig. 6 Comprehensive optical characterization and performance analysis of the photocatalytic composite nanofiber membranes. (a) UV-vis diffuse reflectance spectroscopy (DRS) results and (b) band gap estimations derived from Tauc plots for NFs, RE-NFs, and La-doped RE-NFs. (c) Photoluminescence (PL) spectra under UV excitation at 300 nm demonstrating electron–hole recombination rates. (d) Photocatalytic degradation efficiency of CR under various scavengers. (e) Reusability tests of La-doped RE-NFs showing their photocatalytic activity over five consecutive cycles. (f) Comparison of CR degradation under photolysis (UV irradiation without a photocatalyst), hydrothermally treated nanofibers (h-NFs), untreated NFs, and La-doped RE-NFs.

comparable to that of ZnO/Ag_2O on PVDF, which showed a rate of $0.148 \ min^{-1} \ g^{-1}$ for methylene blue (MB) using a 6 W UV lamp. Despite higher rate constants reported for other materials such as $Bi_2O_2CO_3$–BiOI on PAN ($0.16 \ min^{-1} \ g^{-1}$) and $CoFe_2O_4$/BiOI on PVP ($2.83 \ min^{-1} \ g^{-1}$) for Rhodamine B (RhB), these results were obtained using higher power Xe lamps (150–300 W), which could significantly increase energy consumption. The $Ag/BiVO_4/BiPO_4$ composite achieved the highest rate ($0.738 \ min^{-1} \ g^{-1}$) for tetracycline (TC) but required a 150 W Xe lamp. The key advantage of

the La-doped RE-NFs lies in their effective degradation performance with lower power UV lamps, making them more suitable for energy-efficient and sustainable water treatment. Additionally, the La-doped RE-NFs demonstrated excellent reusability with minimal loss in activity over multiple cycles, unlike many conventional powdered photocatalysts, which often face challenges such as agglomeration and difficult recovery.

The optical properties of the nanofiber composites are critical in determining their suitability and efficiency in

Table 1 Comparison of various photocatalysts integrated into nanofiber matrices for the degradation of different pollutants under UV or Xe lamp irradiation (PAN = polyacrylonitrile, PVP = polyvinylpyrrolidone, PVDF = Polyvinylidene fluoride)

Photocatalysts	Polymer matrix	Pollutants	Lamp type	Kinetics	Kinetics per g	Ref.
$Bi_2O_2CO_3$–BiOI	PAN	RhB	300 W Xe lamp	$0.016 \ min^{-1}$@100 mg	$0.16 \ min^{-1} \ g^{-1}$	77
SiO_2@g-C_3N_4/BiOI	PVP	RhB	150 W Xe lamp	$0.0154 \ min^{-1}$@30 mg	$0.51 \ min^{-1} \ g^{-1}$	78
$CoFe_2O_4$/BiOI	PVP	RhB	300 W Xe lamp	$0.0283 \ min^{-1}$@10 mg	$2.83 \ min^{-1} \ g^{-1}$	79
ZnO/Ag_2O	PVDF	MB	6 W UV lamp	$0.0148 \ min^{-1}$@100 mg	$0.148 \ min^{-1} \ g^{-1}$	80
ZnO/CuS	PVDF	MB	6 W UV lamp	$0.00653 \ min^{-1}$@100 mg	$0.065 \ min^{-1} \ g^{-1}$	81
Nb_2O_5	PAN/PVDF	MB	12 W UV lamp	$0.01296 \ min^{-1}$@150 mg	$0.086 \ min^{-1} \ g^{-1}$	15
$Ag/BiVO_4/BiPO_4$	PVP	TC	150 W Xe lamp	$0.0369 \ min^{-1}$@50 mg	$0.738 \ min^{-1} \ g^{-1}$	82
PCNFs@TiO_2–CuTCP	PAN	RhB	300 W Xe lamp	$0.0115 \ min^{-1}$@10 mg	$1.15 \ min^{-1} \ g^{-1}$	83
$BiOBr/W_{18}O_{49}$	PAN	RhB	300 W Xe lamp	$0.058 \ min^{-1}$@20 mg	$2.9 \ min^{-1} \ g^{-1}$	84
La-doped RE-NFs	PAN/PVDF	CR	4×10 W UV lamp	$0.00753 \ min^{-1}$@50 mg	$0.15 \ min^{-1} \ g^{-1}$	This Study

photocatalytic applications. Fig. 6(a) and (b) from the UV-vis DRS and Tauc plot analyses, respectively, provide insight into how the optical characteristics of the nanofibers influence their photodegradation capabilities. Fig. 6(a) shows the reflectance spectra of NFs, RE-NFs, and La-doped RE-NFs across the UV-Vis wavelength range. The Tauc plot in Fig. 6(b) is used to estimate the optical band gap of the nanofiber composites.[85,86] This plot, which represents the square root of the product of the absorption coefficient and the photon energy $[(F(R_\infty)hv)^{\frac{1}{2}}]$ versus photon energy (hv), allows for the determination of the band gap by extrapolating the linear portion of the plot to the energy axis. The intercepts on the energy axis give the band gap energies of the materials. From the plot, it is evident that the La-doped RE-NFs exhibit a smaller band gap (3.47 eV) compared to NFs (4.81 eV) and RE-NFs (3.53 eV). These values confirm that all nanofibers are primarily activated by UV light. Despite the band gaps remaining in the UV range, the slight reduction in the band gap for La-doped RE-NFs implies a marginal shift towards the visible range, which may slightly broaden their photocatalytic activity under sunlight. Nonetheless, the primary activation remains in the UV region, aligning with the photodegradation results, which indicate enhanced performance under UV light conditions.

Fig. 6(c) presents the photoluminescence (PL) spectra of NFs, RE-NFs, and La-doped RE-NFs, which provide insights into the recombination dynamics of photogenerated electron–hole pairs—a key factor influencing photocatalytic efficiency. A lower PL intensity typically indicates reduced electron–hole recombination, leading to improved charge separation and enhanced photocatalytic activity.[87–89] The PL spectra shows that La-doped RE-NFs exhibit the lowest intensity compared to NFs and RE-NFs, suggesting that La incorporation effectively suppresses electron–hole recombination. This enhanced charge separation allows more charge carriers to participate in photocatalytic reactions, thereby improving pollutant degradation performance. Furthermore, the improved charge separation efficiency in La-doped RE-NFs aligns with the band gap analysis. The slightly reduced band gap (3.47 eV) compared to NFs (4.81 eV) and RE-NFs (3.53 eV) enables more effective photon absorption in the UV region. This combination of enhanced light absorption and suppressed recombination supports the superior photocatalytic activity observed in La-doped RE-NFs under UV irradiation. The lower PL intensity also suggests an extended carrier lifetime, further enhancing the material's photocatalytic performance. Previous findings have also confirmed the enhanced performance of photocatalysts due to electron–hole separation, trapping, and interfacial charge transfer via femtosecond transient absorption spectroscopy (fs-TAS).[90,91]

The scavenger experiment, illustrated in Fig. 6(d), utilized CR as the model dye to investigate the primary reactive species involved in photocatalytic degradation. The degradation efficiency of CR was measured in the presence of various scavengers, and the results revealed significant differences in degradation behavior. Without any scavengers, the degradation percentage reached 61.4%, serving as the baseline for comparison. When p-benzoquinone (BQ) was added to capture

superoxide radicals ($^\bullet O_2^-$), the degradation efficiency dropped to −6.9%, indicating that superoxide radicals are the dominant species responsible for the degradation process. In the presence of ethylenediaminetetraacetic acid (EDTA), which targets photogenerated holes (h^+), the degradation efficiency was 33.7%, showing that h^+ also plays an important, albeit secondary, role. The effect of tert-butanol (T-Bu), which scavenges hydroxyl radicals ($^\bullet OH$), resulted in a degradation efficiency of 50.9%, indicating that $^\bullet OH$ radicals contribute less to the photocatalytic activity in this system. These results suggest that superoxide radicals are the key species driving the photocatalytic degradation of CR, with photogenerated holes also contributing, while hydroxyl radicals play a minor role.[92–94]

The reusability of the La-doped RE-NFs was tested over five consecutive photocatalytic degradation cycles, as shown in Fig. 6(e). The degradation efficiency values for the five cycles are 61.41%, 61.82%, 62.69%, 61.86%, and 58.38%, respectively. These results demonstrate that the photocatalyst maintained high efficiency across multiple uses, with only a slight decrease in performance by the fifth cycle. Specifically, the degradation efficiency dropped by approximately 4.94% after the fifth cycle compared to the first cycle, indicating that the La-doped RE-NFs exhibit excellent stability and reusability. The ease of reusing photocatalytic membrane is a clear advantage over conventional powder-based photocatalyst, which often faces challenging issues (e.g., agglomeration, loss of activity, and difficulty in recovery after repeated use).[95,96] The durability and efficient reusability of the La-doped RE-NFs highlight their potential for practical applications in long-term water treatment processes.

Fig. 6(f) compares the photolysis, hydrothermally treated nanofibers (h-NFs), NFs, and La-doped RE-NFs for the degradation of 10 ppm CR solution under UV irradiation. The photolysis experiment, where CR was exposed to UV light without a photocatalyst, shows a slow and limited reduction in concentration, indicating that direct UV exposure alone contributes minimally to degradation. Similarly, h-NFs (PAN/PVDF nanofibers subjected to hydrothermal treatment without $Ce(NO_3)_3 \cdot 6H_2O$ and urea) and NFs exhibit only a moderate improvement, suggesting that neither the polymer matrix nor hydrothermal treatment alone significantly enhances photocatalytic activity. In contrast, the La-doped RE-NFs demonstrate a rapid decline in CR concentration. This significant difference confirms that La-doped RE-NFs actively enhance photocatalytic efficiency by promoting charge separation and generating reactive oxygen species (ROS), leading to much faster CR degradation compared to photolysis, h-NFs, and untreated NFs.

Proposed photocatalytic degradation mechanism

The proposed photocatalytic mechanism of the La-doped RE-NFs for degrading organic pollutants under UV light is illustrated in Fig. 7. When the La-doped RE-NFs are exposed to UV light, electrons (e^-) are excited from the valence band (VB) to the conduction band (CB), leaving behind holes (h^+) in the VB. The separation of these electron–hole pairs is enhanced by the presence of lanthanum, which helps to reduce the recombination

Fig. 7 Proposed photocatalytic mechanism for La-doped RE-NFs under UV light irradiation. The La-doped RE-NFs absorb UV light.

rate (see Fig. 6c) and facilitates the generation of reactive oxygen species (ROS). The photogenerated electrons react with dissolved oxygen (O_2) molecules in the surrounding solution to produce superoxide radicals ($\bullet O_2^-$), while the holes oxidize water (H_2O) or hydroxide ions (OH^-) to generate hydroxyl radicals ($\bullet OH$). These ROS are highly reactive and play a critical role in breaking down complex organic pollutants into smaller, harmless molecules like CO_2 and H_2O.[97–99] The scavenger analysis further supports this mechanism, highlighting the specific contributions of different ROS in the degradation process. The addition of *p*-benzoquinone (BQ), a scavenger for ($\bullet O_2^-$), resulted in a significant drop in degradation efficiency, even showing negative values due to inhibited photocatalytic activity, indicating that superoxide radicals are the primary active species responsible for pollutant breakdown. Meanwhile, the use of ethylenediaminetetraacetic acid (EDTA), which captures h^+, led to a moderate reduction in degradation efficiency, suggesting that photogenerated holes also contribute to the process. The presence of *tert*-butanol (T-Bu), a scavenger for $\bullet OH$, showed a less pronounced effect on the degradation, indicating a secondary role of hydroxyl radicals in the photocatalytic process. Beyond the improved activity due to effective ROS generation, the La-doped RE-NFs also offer significant advantages as a membrane-based catalyst. Unlike traditional powdered photocatalysts, the nanofiber membrane structure ensures easier recovery and reuse, avoiding the common issues of catalyst loss and agglomeration. The high surface area of the nanofibers enhances interaction with pollutants, improving overall reaction efficiency. Additionally, the stability of the membrane allows for consistent performance over multiple cycles, making it a more sustainable solution for long-term water treatment applications. The combination of efficient ROS generation, lanthanum-enhanced charge separation, and practical benefits of the membrane structure has positioned the La-doped RE-NFs as a superior alternative for photocatalytic water purification.

The incorporation of lanthanum (La) in the rare-earth nanofiber composite (La-doped RE-NFs) plays a crucial role in enhancing structural stability, crystallinity, charge separation, and photocatalytic efficiency. TGA results (Fig. 3d) indicate that La-doped RE-NFs exhibit higher thermal stability, with a residual weight of 60.6% at 600 °C, suggesting that La enhances the formation of stable inorganic phases and strengthens polymer-metal oxide interactions. Additionally, XRD analysis (Fig. 3b) reveals that the $CeCO_3F$ phase in La-doped RE-NFs is more crystalline, indicating that La may facilitate the ordered growth of $CeCO_3F$ on the nanofiber surfaces, which can improve charge carrier mobility and stability. Furthermore, photoluminescence (PL) spectra (Fig. 6c) show that La-doped RE-NFs exhibit lower PL intensity, suggesting reduced electron–hole recombination and improved charge separation efficiency, allowing more charge carriers to participate in photocatalytic reactions, thereby leading to enhanced photocatalytic performance.[100,101]

Conclusions

Lanthanum-doped hierarchical rare-earth metal oxide composite nanofiber membranes (La-doped RE-NFs) with superior photocatalytic performance and high reusability have been successfully developed by combining electrospinning and hydrothermal synthesis methods. The La-doped RE-NFs demonstrated enhanced photocatalytic activity for the degradation of various organic water pollutants (*i.e.*, Congo red (CR), methyl orange (MO), methylene blue (MB), and tetracycline (TC)). The FE-SEM images clearly highlighted the growth of nanorod structures on top of the nanofiber surfaces, which significantly increased the surface area and contributed to the material's superior photocatalytic performance. Additionally, XRD and XPS analysis revealed the formation of the $CeCO_3F$ phase as the dominant structure, providing further evidence of successful material synthesis under hydrothermal conditions. This phase formation, although unexpected, likely contributed to the improved photocatalytic activity of the composite. The photocatalytic degradation experiments demonstrated a significant enhancement in the performance of La-doped RE-NFs across various pollutants. The first-order kinetic plots revealed a marked increase in the degradation rate constants (k) for La-doped RE-NFs compared to the NFs and RE-NFs. The rate constant for MB degradation exhibited an even more pronounced improvement, with La-doped RE-NFs achieving a 4.3-fold increase over NFs. These enhancements in the k-values across all pollutants underscore the effectiveness of lanthanum doping in accelerating

photocatalytic reactions and improving overall degradation efficiency. The reusability of La doped RE-NFs was demonstrated across five cycles of photocatalytic degradation, with only a 4.94% reduction in efficiency after multiple uses. The membrane-based photocatalyst's stability and easy recovery offer significant advantages over traditional powder photocatalysts, which often face challenges such as agglomeration and difficulty in recovery. The findings of this study indicate that La-doped RE-NFs represent a highly efficient, stable, and reusable photocatalytic material for environmental remediation, particularly in the degradation of organic pollutants in water treatment systems. Future research shall focus on optimizing doping concentrations and exploring the material's photocatalytic behavior under visible light to expand its application beyond UV irradiation. Additionally, scaling up the synthesis process and conducting real-world tests in complex pollutant mixtures will help assess the practical viability of this material in industrial water treatment systems.

Author contributions

Aditya Rianjanu: conceptualization, methodology, investigation, writing – original draft, writing – review & editing, visualization, supervision, funding acquisition. Sephia Amanda Muhtar: investigation. Hannah Faye M. Austria: investigation. Tarmizi Taher: investigation, writing – review & editing. Noto Susanto Gultom: resources, formal analysis. Wibawa Hendra Saputera: resources. Hutomo Suryo Wasisto: validation, writing – review & editing. Fatwa F. Abdi: validation, writing – review & editing. Wei-Song Hung: supervision, funding acquisition. Januar Widakdo: conceptualization, writing – review & editing, supervision, resources, funding acquisition. All authors approved the final manuscript.

Data availability

The data supporting this article has been included as part of the ESI.†

Conflicts of interest

The authors declare that there are no conflicts of interest.

Acknowledgements

References

1 W. Guo, T. Guo, Y. Zhang, L. Yin and Y. Dai, *Chemosphere*, 2023, **339**, 139486.

2 H. Wu, L. Li, S. Wang, N. Zhu, Z. Li, L. Zhao and Y. Wang, *Phys. Chem. Chem. Phys.*, 2023, **25**, 25899–25924.

3 H. Zhou, H. Wang, C. Yue, L. He, H. Li, H. Zhang, S. Yang and T. Ma, *Appl. Catal., B*, 2024, **344**, 123605.

4 J. Prakash, P. Kumar, N. Saxena, Z. Pu, Z. Chen, A. Tyagi, G. Zhang and S. Sun, *J. Mater. Chem. A*, 2023, **11**, 10015–10064.

5 Z. H. Jabbar, B. H. Graimed, S. H. Ammar, D. A. Sabit, A. A. Najim, A. Y. Radeef and A. G. Taher, *Mater. Sci. Semicond. Process.*, 2024, **173**, 108153.

6 K. Bano, S. K. Mittal, P. P. Singh and S. Kaushal, *Nanoscale Adv.*, 2021, **3**, 6446–6458.

7 M. Rani, K. Keshu, S. Pandey, R. Rishabh, S. Sharma and U. Shanker, *J. Photochem. Photobiol., A*, 2024, **446**, 115160.

8 T. Velempini, E. Prabakaran and K. Pillay, *Mater. Today Chem.*, 2021, **19**, 100380.

9 M. Utami, A. Rianjanu, M. M. Musawwa, S. C. Nur, P. Lestari, F. S. Al-Khattaf, A. A. Hatamleh, M. Chandrasekaran, W. J. Chung, S. W. Chang and B. Ravindran, *Environ. Geochem. Health*, 2024, **46**, 378.

10 F. M. Sanakousar, C. C. Vidyasagar, V. M. Jiménez-Pérez and K. Prakash, *Mater. Sci. Semicond. Process.*, 2022, **140**, 106390.

11 M. Yoga Darmawan, N. Imani Istiqomah, N. Adrianto, R. Marsel Tumbelaka, A. Dwi Nugraheni and E. Suharyadi, *Results Chem.*, 2023, **6**, 100999.

12 H. Aliah, N. Puspita Rini, I. Syafar Farouk, Z. Zurnansyah, L. Jestha Mahardhika, P. Dwi Jayanti, H. Perdana Kusumah, R. Marsel Tumbelaka, N. Imani Istiqomah, N. Sumawati Asri, R. Nur Iman and E. Suharyadi, *Carbon Resour. Convers.*, 2024, **7**, 100235.

13 V. Dutta, S. Sharma, P. Raizada, V. K. Thakur, A. A. P. Khan, V. Saini, A. M. Asiri and P. Singh, *J. Environ. Chem. Eng.*, 2021, **9**, 105018.

14 M. G. Peleyeju and E. L. Viljoen, *J. Water Process Eng.*, 2021, **40**, 101930.

15 A. Rianjanu, K. D. P. Marpaung, E. K. A. Melati, R. Aflaha, Y. G. Wibowo, I. P. Mahendra, N. Yulianto, J. Widakdo, K. Triyana, H. S. Wasisto and T. Taher, *Nano Mater. Sci.*, 2024, **6**, 96–105.

16 A. Rianjanu, S. A. Muhtar, C. Siburian, K. D. P. Marpaung, R. Aflaha, S. E. M. Putra, A. Afandi, K. Triyana, F. F. Abdi, T. Taher and H. S. Wasisto, *Adv. Eng. Mater.*, 2025, 2402287.

17 K. Su, H. Liu, Z. Gao, P. Fornasiero and F. Wang, *Adv. Sci.*, 2021, **8**, 2003156.

18 A. Rianjanu, A. S. P. Mustamin, E. K. A. Melati, R. Aflaha, N. I. Khamidy, M. Utami, K. Khairurrijal, K. Triyana, F. F. Abdi, H. S. Wasisto and T. Taher, *Colloids Surf., A*, 2024, **682**, 132919.

19 A. Rianjanu, K. D. P. Marpaung, C. Siburian, S. A. Muhtar, N. I. Khamidy, J. Widakdo, N. Yulianto, R. Aflaha, K. Triyana and T. Taher, *Results Eng.*, 2024, **23**, 102748.

20 A. Rianjanu, T. Haloho, J. L. Pasaribu, A. G. Fahmi, E. Nurfani, W. S. Sipahutar, H. T. Yudistira and T. Taher, *Sci. Technol.*, 2025, **10**, 123–130.

21 A. Rianjanu, R. Nuraeni, R. Aflaha, N. I. Khamidy, K. Triyana and T. Taher, *Greensusmater*, 2024, **1**, 9–14.

22 I. J. Budiarso, V. A. Dabur, R. Rachmantyo, H. Judawisastra, C. Hu and A. Wibowo, *Mater. Adv.*, 2024, **5**, 2668–2688.

23 X. Wang, J. Zhang, H. Wang, M. Liang, Q. Wang and F. Chen, *Energy Environ. Mater.*, 2024, **7**, e12616.

24 C. Zhou, L. Huang, Z. Chen, Y. Zhang, J. Chen, J. Li, X. Zhou, H. Abdelsalam and Q. Zhang, *J. Alloys Compd.*, 2024, **988**, 174219.

25 H. Pérez del Pulgar, J. Ortiz-Bustos, S. Gómez-Ruiz, I. del Hierro and Y. Pérez, *Environ. Sci.*, 2024, **10**, 2087–2102.

26 M. B. Chabalala, B. M. Mothudi and B. Ntsendwana, *J. Photochem. Photobiol., A*, 2024, **447**, 115244.

27 M. S. Khan, Y. Li, D.-S. Li, J. Qiu, X. Xu and H. Y. Yang, *Nanoscale Adv.*, 2023, **5**, 6318–6348.

28 B. Sarkodie, J. Amesimeku, C. Frimpong, E. K. Howard, Q. Feng and Z. Xu, *Chemosphere*, 2023, **313**, 137654.

29 M. Badmus, J. Liu, N. Wang, N. Radacsi and Y. Zhao, *Nano Mater. Sci.*, 2021, **3**, 213–232.

30 M. Kardeş, H. C. Yatmaz and K. Öztürk, *ACS Appl. Nano Mater.*, 2023, **6**, 6605–6613.

31 S. Wang, Y. Zhang, T. Zhang, F. Dong and H. Huang, *Appl. Catal., B*, 2017, **208**, 75–81.

32 S. Teixeira, P. M. Martins, S. Lanceros-Méndez, K. Kühn and G. Cuniberti, *Appl. Surf. Sci.*, 2016, **384**, 497–504.

33 D. Xiong, W. Zhao, J. Guo, S. Li, Y. Ye, L. E and X. Yang, *Sep. Purif. Technol.*, 2021, **277**, 119628.

34 E. Valadez-Renteria, J. Oliva and V. Rodriguez-Gonzalez, *Sci. Total Environ.*, 2022, **807**, 150820.

35 I. Kolesnyk, J. Kujawa, H. Bubela, V. Konovalova, A. Burban, A. Cyganiuk and W. Kujawski, *Sep. Purif. Technol.*, 2020, **250**, 117231.

36 J. Zhang, H. Wu, L. Shi, Z. Wu, S. Zhang, S. Wang and H. Sun, *Sep. Purif. Technol.*, 2024, **329**, 125225.

37 C. Zang, H. Chen, X. Han, W. Zhang, J. Wu, F. Liang, J. Dai, H. Liu, G. Zhang, K.-Q. Zhang and M. Ge, *RSC Adv.*, 2022, **12**, 34107–34116.

38 P. Fourmont, R. Nechache and S. G. Cloutier, *ACS Appl. Nano Mater.*, 2021, **4**, 12261–12269.

39 F. Huang, S. Guo, Y. Yan, W. Zhang, J. Cao, G. Li and Y. Ji, *Sep. Purif. Technol.*, 2023, **325**, 124672.

40 S. Hartati, A. Zulfi, P. Y. D. Maulida, A. Yudhowijoyo, M. Dioktyanto, K. E. Saputro, A. Noviyanto and N. T. Rochman, *ACS Omega*, 2022, 7, 10516–10525.

41 M. F. Arif, S. A. Muhtar, C. Siburian, K. D. P. Marpaung, N. Yulianto, F. F. Abdi, T. Taher, H. S. Wasisto and A. Rianjanu, *Case Stud. Chem. Environ. Eng.*, 2024, **10**, 100806.

42 Z. Yao, M. Xia, Z. Xiong, Y. Wu, P. Cheng, Q. Cheng, J. Xu, D. Wang and K. Liu, *ACS Omega*, 2022, 7, 3030–3036.

43 D. Wang, K. Wan, M. Zhang, H. Li, P. Wang, X. Wang and J. Yang, *Sens. Actuators, B*, 2019, **283**, 714–723.

44 G. Zhang, J. Sun, D. Chen, N. Li, Q. Xu, H. Li, J. He and J. Lu, *J. Hazard. Mater.*, 2020, **398**, 122889.

45 M. Zhang, D. Yang, S. Zhang, T. Xu, Y. Shi, Y. Liu, W. Chang and Z.-Z. Yu, *Carbon*, 2020, **158**, 873–884.

46 L. Kong, Y. Wang, C. B. Andrews and C. Zheng, *Chem. Eng. J.*, 2022, **435**, 134830.

47 W. Feng, Y. Chen, W. Wang and D. Yu, *Colloids Surf., A*, 2022, **633**, 127890.

48 S. Kang, D. Hoon Park and J. Hwang, *J. Hazard. Mater.*, 2022, **424**, 127262.

49 T. Yang, H. Pan, G. Tian, B. Zhang, D. Xiong, Y. Gao, C. Yan, X. Chu, N. Chen, S. Zhong, L. Zhang, W. Deng and W. Yang, *Nano Energy*, 2020, **72**, 104706.

50 G. Montes-Hernandez, R. Chiriac, N. Findling, F. Toche and F. Renard, *Mater. Chem. Phys.*, 2016, **172**, 202–210.

51 N. Li, S. Zhang, Z. Cheng and W. Wu, *RSC Adv.*, 2021, **11**, 27607–27619.

52 S. He, K. Zhang, Z. Meng and Y. Li, *Mol. Catal.*, 2024, **569**, 114636.

53 J. Dong, X. Wang, L. Song, J. Yang, H. Wu, C. Yang and S. Gan, *Dalton Trans.*, 2018, **47**, 15061–15070.

54 L. Pan, Y. Wang, Q. Jin, Z. Hu, Z. Zhou and M. Zhu, *Chem. Eng. J.*, 2024, **479**, 147742.

55 Z. Mokhtari-Shourijeh, S. Langari, L. Montazerghaem and N. M. Mahmoodi, *J. Environ. Chem. Eng.*, 2020, **8**, 103876.

56 Y. Chen and L. Jiang, *Appl. Water. Sci.*, 2021, **11**, 51.

57 Y. Zou, S. Jiang, X. Hu, W. Xu, Z. Chen, K. Liu and H. Hou, *Mater. Today Commun.*, 2021, **26**, 102069.

58 L.-L. I. Fockaert, D. Ganzinga-Jurg, J. Versluis, B. Boelen, H. J. Bakker, H. Terryn and J. M. C. Mol, *J. Phys. Chem. C*, 2020, **124**, 7127–7138.

59 R. Venkataswamy, L. Trimble, S. Ryu, N.-T. Le, K. Park, H. Kang and J. Seo, *Ceram. Int.*, 2024, **50**, 46032–46041.

60 M. A. Abu-Saied, E. A. El Desouky, M. A. Rafea and M. S. Abusaif, *Mater. Today Commun.*, 2024, **40**, 110232.

61 W. Yao, X. Li, X. Zhu, L. Pei, G. Liu, Y. Cheng, M. O. L. Chee, P. Dong, J. Shen and M. Ye, *Desalination*, 2022, **532**, 115751.

62 H. M. El-Bery, M. R. Salah, S. M. Ahmed and S. A. Soliman, *RSC Adv.*, 2021, **11**, 13229–13244.

63 H. T. T. Le, N. T. Liem, N. C. Giang, P. H. Hoang and N. T. Minh Phuong, *RSC Adv.*, 2023, **13**, 22375–22388.

64 Y.-J. Heo, Y. Zhang, K. Y. Rhee and S.-J. Park, *Composites, Part B*, 2019, **156**, 95–99.

65 Y. Xiao, F. Xiao, W. Ji, L. Xia, L. Li, M. Chen and H. Wang, *J. Membr. Sci.*, 2023, **687**, 122090.

66 N. Li, C. Ren, L. Hou, K. Jiao and W. Wu, *J. Taiwan Inst. Chem. Eng.*, 2023, **152**, 105164.

67 T. Zhang, W. Wang, F. Gu, W. Xu, J. Zhang, Z. Li, T. Zhu, G. Xu, Z. Zhong and F. Su, *Appl. Catal., B*, 2022, **312**, 121385.

68 M. Guo, J. Xiong, X. Jin, S. Lu, Y. Zhang, J. Xu and H. Fan, *J. Membr. Sci.*, 2023, **675**, 121533.

69 P. Liu, L. Wu, X. Huang and Z. Guo, *Surf. Interfaces*, 2024, **46**, 104130.

70 K. Du, R. Tao, C. Guo, H. Li, X. Liu, P. Guo, D. Wang, J. Liang, J. Li, S. Dai and X.-G. Sun, *Nano Energy*, 2022, **103**, 107862.

71 X. Wang, H. Pfeiffer, J. Wei, J. Dan, J. Wang and J. Zhang, *Chem. Eng. J.*, 2022, **428**, 131371.

72 Y. Liu, G. Jiang, L. Li, H. Chen, Q. Huang, X. Du and Z. Tong, *Powder Technol.*, 2017, **305**, 597–601.

73 Y. G. Ko, T. Do, Y. Chun, C. H. Kim, U. S. Choi and J.-Y. Kim, *J. Hazard. Mater.*, 2016, **307**, 91–98.

74 W. Qin, L. Xu, J. Song, R. Xing and H. Song, *Sens. Actuators, B*, 2013, **185**, 231–237.

75 H. D. Tran, D. Q. Nguyen, P. T. Do and U. N. P. Tran, *RSC Adv.*, 2023, **13**, 16915–16925.

76 M. Ateia, M. G. Alalm, D. Awfa, M. S. Johnson and C. Yoshimura, *Sci. Total Environ.*, 2020, **698**, 134197.

77 P. Teng, J. Zhu, Z. Li, K. Li, N. Copner, S. Gao, E. Zhao, X. Zhu, Z. Liu, F. Tian and Y. Zhang, *Opt. Mater.*, 2022, **134**, 112935.

78 X. Wang, X. Zhou, C. Shao, X. Li and Y. Liu, *Appl. Surf. Sci.*, 2018, **455**, 952–962.

79 M.-J. Chang, W.-N. Cui, H. Wang, J. Liu, H.-L. Li, H.-L. Du and L.-G. Peng, *Colloids Surf., A*, 2019, **562**, 127–135.

80 C. Zang, X. Han, H. Chen, H. Zhang, Y. Lei, H. Liu, C. Wang, G. Zhang and M. Ge, *Ceram. Int.*, 2022, **48**, 27379–27387.

81 C. Zang, H. Chen, X. Han, W. Zhang, J. Wu, F. Liang, J. Dai, H. Liu, G. Zhang, K.-Q. Zhang and M. Ge, *RSC Adv.*, 2022, **12**, 34107–34116.

82 J. Zhu, B. Han, Z. Li, C. Chu, X. Yang, P. Teng, S. Gao, E. Zhao, Z. Zhu, F. Tian, H. Jiang, K. Li and N. Copner, *Opt. Mater.*, 2023, **142**, 114133.

83 X. Zhang, Y. Duan, Y. Li, W. Dong, S. Wu and Q. Duan, *Vacuum*, 2023, **218**, 112673.

84 Y. Wang, R. Tao, T. Yan, T. Li, X. Fan, Z. Chu and K. Liu, *Colloids Surf., A*, 2024, **694**, 134054.

85 X. Guo, L. Liu, Y. Xiao, Y. Qi, C. Duan and F. Zhang, *Coord. Chem. Rev.*, 2021, **435**, 213785.

86 Ł. Haryński, A. Olejnik, K. Grochowska and K. Siuzdak, *Opt. Mater.*, 2022, **127**, 112205.

87 M. B. Johnston and L. M. Herz, *Acc. Chem. Res.*, 2016, **49**, 146–154.

88 Y. Kanemitsu, *Acc. Chem. Res.*, 2013, **46**, 1358–1366.

89 Q. Li, M. Anpo and X. Wang, *Res. Chem. Intermed.*, 2020, **46**, 4325–4344.

90 J. Zhang, G. Yang, B. He, B. Cheng, Y. Li, G. Liang and L. Wang, *Chin. J. Catal.*, 2022, **43**, 2530–2538.

91 C. Cheng, J. Zhang, B. Zhu, G. Liang, L. Zhang and J. Yu, *Angew. Chem., Int. Ed.*, 2023, **62**, e202218688.

92 I. J. Ani, U. G. Akpan, M. A. Olutoye and B. H. Hameed, *J. Cleaner Prod.*, 2018, **205**, 930–954.

93 F. Puga, J. A. Navío and M. C. Hidalgo, *Appl. Catal., A*, 2024, **685**, 119879.

94 B. Liu, C. Bie, Y. Zhang, L. Wang, Y. Li and J. Yu, *Langmuir*, 2021, **37**, 14114–14124.

95 H. S. Zakria, M. H. D. Othman, R. Kamaludin, S. H. Sheikh Abdul Kadir, T. A. Kurniawan and A. Jilani, *RSC Adv.*, 2021, **11**, 6985–7014.

96 J. C. Colmenares, R. S. Varma and P. Lisowski, *Green Chem.*, 2016, **18**, 5736–5750.

97 A. Krishnan, A. Swarnalal, D. Das, M. Krishnan, V. S. Saji and S. M. A. Shibli, *J. Environ. Sci.*, 2024, **139**, 389–417.

98 A. Pattnaik, J. N. Sahu, A. K. Poonia and P. Ghosh, *Chem. Eng. Res. Des.*, 2023, **190**, 667–686.

99 D. Li, S. Zhang, S. Li, J. Tang, T. Hua and F. Li, *J. Cleaner Prod.*, 2023, **397**, 136468.

100 S. Zhang, X. Yi, G. Hu, M. Chen, H. Shen, B. Li, L. Yang, W. Dai, J. Zou and S. Luo, *Coord. Chem. Rev.*, 2023, **478**, 214970.

101 D. Kanakaraju, F. D. Anak Kutiang, Y. C. Lim and P. S. Goh, *Appl. Mater. Today*, 2022, **27**, 101500.